



Article

Tris(2-Pyridyl)Arsine as a New Platform for Design of Luminescent Cu(I) and Ag(I) Complexes

Yan V. Demyanov ¹, Evgeniy H. Sadykov ¹, Marianna I. Rakhmanova ¹, Alexander S. Novikov ^{2,3} , Irina Yu. Bagryanskaya ⁴ and Alexander V. Artem'ev ^{1,*} 

¹ Nikolaev Institute of Inorganic Chemistry, SB RAS, 3 Acad. Lavrentiev Ave., 630090 Novosibirsk, Russia

² Saint Petersburg State University, Universitetskaya Nab. 7/9, 199034 Saint Petersburg, Russia

³ Peoples' Friendship University of Russia (RUDN University), Miklukho-Maklaya Street 6, 117198 Moscow, Russia

⁴ N. N. Vorozhtsov Novosibirsk Institute of Organic Chemistry, SB RAS, 9 Acad. Lavrentiev Ave., 630090 Novosibirsk, Russia

* Correspondence: chemisufarm@yandex.ru

Abstract: The coordination behavior of tris(2-pyridyl)arsine (Py₃As) has been studied for the first time on the example of the reactions with CuI, CuBr and AgClO₄. When treated with CuI in CH₂Cl₂ medium, Py₃As unexpectedly affords the scorpionate complex [Cu(Py₃As)I]·CH₂Cl₂ only, while this reaction in MeCN selectively leads to the dimer [Cu₂(Py₃As)₂I₂]. At the same time, the interaction of CuBr with Py₃As exclusively gives the dimer [Cu₂(Py₃As)₂Br₂]. It is interesting to note that the scorpionate [Cu(Py₃As)I]·CH₂Cl₂, upon fuming with a MeCN vapor (r.t., 1 h), undergoes quantitative dimerization into the dimer [Cu₂(Py₃As)₂I₂]. The reaction of Py₃As with AgClO₄ produces complex [Ag@Ag₄(Py₃As)₄](ClO₄)₅ featuring a Ag-centered Ag₄ tetrahedral kernel. At ambient temperature, the obtained Cu(I) complexes exhibit an unusually short-lived photoluminescence, which can be tentatively assigned to the thermally activated delayed fluorescence of (M + X) LCT type (M = Cu, L = Py₃As; X = halogen). For the title Ag(I) complexes, QTAIM calculations reveal the pronounced argentophilic interactions for all short Ag···Ag contacts (3.209–3.313 Å).

Keywords: tris(2-pyridyl)arsine; Cu(I) complexes; Ag(I) clusters; metallophilic interactions; thermally activated delayed fluorescence; dimerization



Citation: Demyanov, Y.V.; Sadykov, E.H.; Rakhmanova, M.I.; Novikov, A.S.; Bagryanskaya, I.Y.; Artem'ev, A.V. Tris(2-Pyridyl)Arsine as a New Platform for Design of Luminescent Cu(I) and Ag(I) Complexes. *Molecules* **2022**, *27*, 6059. <https://doi.org/10.3390/molecules27186059>

Academic Editors: M. Concepción Gimeno and Wei-Yin Sun

Received: 23 August 2022

Accepted: 8 September 2022

Published: 16 September 2022

Publisher's Note: MDPI stays neutral with regard to jurisdictional claims in published maps and institutional affiliations.



Copyright: © 2022 by the authors. Licensee MDPI, Basel, Switzerland. This article is an open access article distributed under the terms and conditions of the Creative Commons Attribution (CC BY) license (<https://creativecommons.org/licenses/by/4.0/>).

1. Introduction

Over the past decade, luminescent Cu(I) and Ag(I) complexes have attracted a considerable attention due to their intriguing structural diversity [1–11] and ability to exhibit efficient phosphorescence or thermally activated delayed fluorescence (TADF) [12–19], or even dual emission [20,21]. Owing to these features, such compounds are now considered as promising emitters for energy-efficient OLEDs of second and third generations (PHOLED and TADF OLED) [22,23], just as for light-emitting electrochemical cells (LEECs) [24]. Moreover, Cu(I) and Ag(I) complexes are reported to be perspective luminescent sensors and X-ray scintillators, as well as “smart” materials, the emission of which is sensitive to the external stimuli (temperature, pressure, chemicals) [25–28].

To design luminescent Cu(I) and Ag(I) complexes, various C-, N-, and P-donor ligands such as carbenes, azaheterocycles, and phosphines are commonly exploited [29–34]. At that, “heavy pnictine(III)”-based ligands, e.g., arsines, remain almost unexplored in this regard. Meanwhile, recent studies [35–37] have demonstrated that the arsine ligands can be preferable over similar phosphines to fabricate Cu(I)-based TADF materials [38]. Indeed, the higher spin-orbital coupling (SOC) strength of arsenic ($\zeta_1 = 1202 \text{ cm}^{-1}$) [39] against phosphorus ($\zeta_1 = 230 \text{ cm}^{-1}$) [39] makes the emission rate of Cu(I)-arsine complexes much faster compared to that of similar Cu(I)-phosphine derivatives [38]. Considering that the triplet or TADF emitters with short decay times ($<2 \mu\text{s}$) are essential for OLED

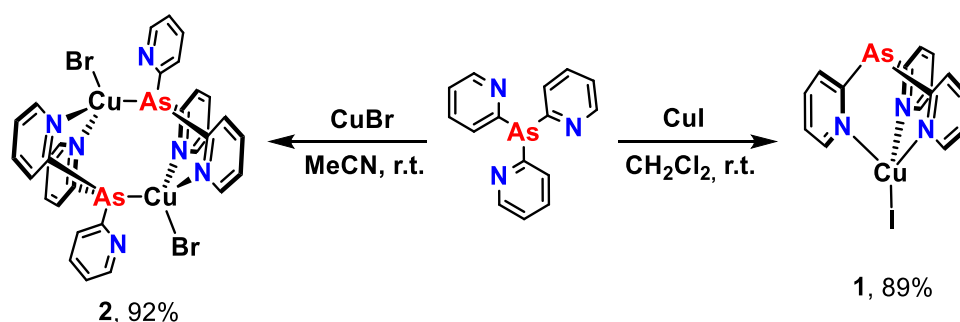
related applications, the design of new Cu(I)-arsine complexes, just as their Ag(I) congeners, represents a daunting challenge.

Working in this field, we have paid attention to pyridylarsines, “heavy pnictogen” analogs of pyridylphosphines. The latter are a famous family of ligands which are widely used for the design of Cu(I) and Ag(I) complexes showing very efficient TADF or/and phosphorescence [40–44]. The survey of the literature reveals, however, that the azaheterocyclic-substituted arsines are very limited in number [45–47], and their Cu(I)/Ag(I) derivatives are even scarcer [38,46,47]. Herein, for the first time, we have employed tris(2-pyridyl)arsine as a stabilizing platform for Cu(I) and Ag(I) complexes. The latter have been studied in terms of solid-state luminescence, thermal stability and electronic structure.

2. Results and Discussion

2.1. Synthesis and Characterization

It was reported that tris(2-pyridyl)phosphine (Py₃P) reacted with Cu(I) halides to irreversibly give air-stable dimeric complexes [Cu₂(Py₃P)₂X₂] (X = Cl, Br, I) in high yields [48]. Therefore, it would be reasonable to expect that Py₃As could also give the related complexes. Meanwhile, we have found that the reactivity of Py₃As differs from that of Py₃P. Namely, CuI easily reacts with Py₃As in CH₂Cl₂ to furnish the unexpected scorpionate [Cu(Py₃As)I] (**1**) only, isolated as a solvate **1**·CH₂Cl₂ in 89% yield (Scheme 1). By contrast, CuBr under similar conditions affords a dimeric complex [Cu₂(Py₃As)₂Br₂] (**2**) in 92% yield. Our numerous attempts to synthesize CuBr-based scorpionate under the varied conditions (different Cu/Py₃As ratios, diverse solvents) failed: complex **2** was already formed in all the experiments. Of note, CuCl also easily reacts with Py₃As, but a product formed was found to be easily oxidized in air to produce unidentified green Cu(II) complexes.



Scheme 1. Reactions of Py₃As with CuBr and CuI.

To explain the different reactivity of Py₃As towards CuBr and CuI, the dimerization energies for the equilibria 2[Cu(Py₃As)X] ↔ [Cu₂(Py₃As)₂X₂] (X = Br, I) have been assessed at the PBE0/def2-TZVP level of the theory. The performed calculations reveal that the formation of a dimer is indeed thermodynamically more preferable for X = Br by 2.34 kcal·mol^{−1}, whereas scorpionate is favorable for X = I by 0.97 kcal·mol^{−1} (Supplementary Materials, Figure S10). It should be noted, however, that an additional stabilization of scorpionate [Cu(Py₃As)I] in **1**·CH₂Cl₂ is possible through the solvate molecules (*vide infra*).

Our attempts to transform **2** into scorpionate [Cu(Py₃As)Br] using recrystallization from different solvents failed. Meanwhile, we have found that the fuming of **1**·CH₂Cl₂ with MeCN vapor (23 °C, 1 h) results in quantitative and irreversible dimerization into [Cu₂(Py₃As)₂I₂] (Figure 1a). The reaction is accompanied by the changing of the parent emission color of **1** (*vide infra*) to green, which is specific for complexes of [Cu₂(Py₃As)₂X₂] type (X = P or As). The powder X-ray diffraction (PXRD) pattern of the product [Cu₂(Py₃As)₂I₂], differs from that of [Cu₂(Py₃As)₂Br₂] (**2**), but closely resembles that of a similar phosphine derivative, [Cu₂(Py₃P)₂Br₂] (Figure 1b). Since the attempts to grow X-ray quality crystals of **1a** met with no success, its structure has been proved by PXRD, mid-IR and ¹H NMR data only. Eventually, we have found that complex **1a** can be successfully synthesized in an

almost quantitative yield by the straightforward reaction of Py_3As with CuI in MeCN (r.t., 10 min) (Figure 1a). Thus, a noticeable effect of solvents on the reaction outcome has been established for the reaction of Py_3As with CuI .

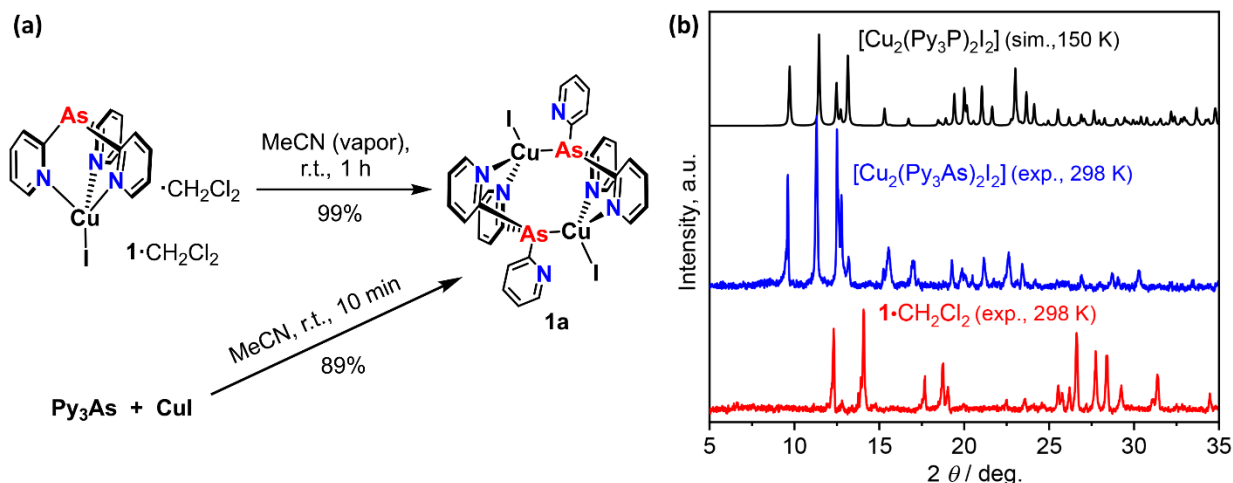
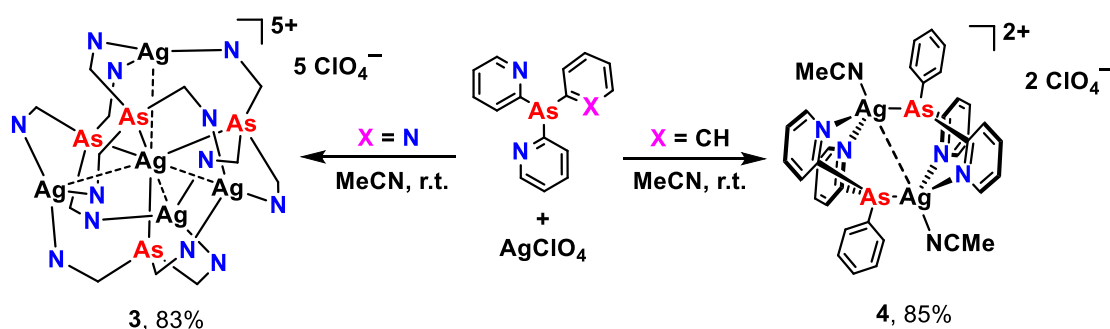


Figure 1. (a) MeCN -driven dimerization of **1**, and direct interaction of Py_3As with CuI in MeCN ; (b) associated changing in PXRD patterns: experimental diffractograms of starting complex **1** (down curve), product **1a** (middle curve), and simulated PXRD pattern for $[\text{Cu}_2(\text{Py}_3\text{P})_2\text{I}_2]$ (top curve).

In the next step, we have examined the complexation of Py_3As with Ag(I) using AgClO_4 as a precursor. The reaction easily occurs in MeCN medium, and the following recrystallization of the product in water produces a four-nuclear cluster $[\text{Ag}@\text{Ag}_4(\text{Py}_3\text{As})_4](\text{ClO}_4)_5 \cdot 3\text{H}_2\text{O}$ ($3 \cdot 3\text{H}_2\text{O}$) in high yield (Scheme 2). Of note, the same product is also formed even when the $\text{AgClO}_4/\text{Py}_3\text{As}$ molar ratio deviates from the stoichiometric one (5:4) being 1:1, 2:1, or 1:2. For comparison, the reaction of bis(2-pyridyl)phenylarsine (Py_2PhAs) with AgClO_4 under similar conditions has also been implemented to deliver a dinuclear complex $[\text{Ag}_2(\text{Py}_2\text{PhAs})_2(\text{MeCN})_2](\text{ClO}_4)_2 \cdot \text{CH}_3\text{CN}$ ($4 \cdot \text{CH}_3\text{CN}$), the structure of which resembles that of **2**. Again, the $\text{AgClO}_4/\text{Py}_2\text{PhAs}$ ratio does not affect the reaction outcome: only complex **2** is formed.



Scheme 2. Reactivity of Py_3As and Py_2PhAs in reactions with AgClO_4 .

The X-ray derived structures of the prepared complexes are displayed in Figure 2, and the selected interatomic distances are listed in Table 1. In the structure of **1**· CH_2Cl_2 (Figure 2), the Cu atom is coordinated by Py_3As in a $\text{N}, \text{N}', \text{N}''$ -tripodal manner, and the iodine atom completes a distorted tetrahedral environment of the metal ($\tau_4 = 0.85$) [49]. Note that the iodine atom of **1** deviates from the axis passing from As and Cu atoms by only 0.8° , unlike the similar complex with tris(2-pyridyl)arsine oxide, where such deviation reaches 9.4° [50]. The dihedral angles between averaged pyridine planes of **1** are $\approx 114.3^\circ$, 114.4° and 131.2° .

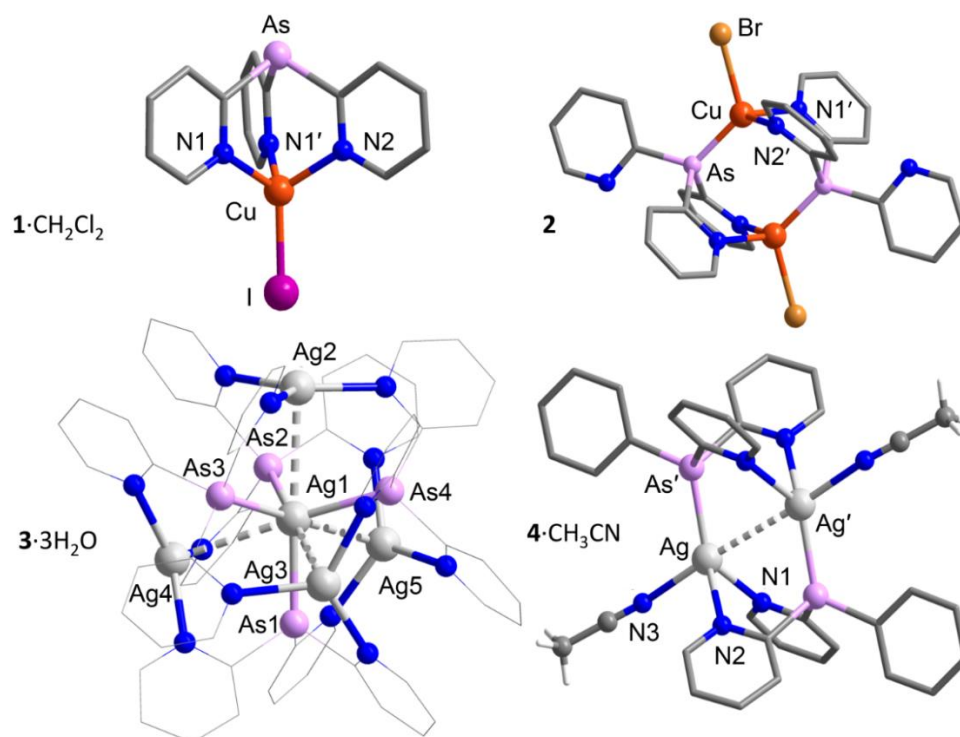


Figure 2. X-ray derived structures of **1**·CH₂Cl₂, **2**, **3**·3H₂O (one of three independent parts) and **4**·CH₃CN. The aromatic H atoms, solvate molecules and counterions are omitted for clarity.

Table 1. Selected bond lengths (Å) and angles (°) for **1**·CH₂Cl₂, **2**, **3**·3H₂O and **4**·CH₃CN.

1·CH ₂ Cl ₂		2	
Cu–N2	2.046(3)	Cu–As	2.3207(5)
Cu–N1	2.042(2)	Cu–N1′	2.051(3)
Cu–N1′	2.042(2)	Cu–N2′	2.066(2)
Cu–I	2.5003(6)	Cu–Br	2.4242(6)
Symmetry code: (′) x, y, z–1/2.		Symmetry code: (′) 1–x, 1–y, 1–z.	
3·3H ₂ O		4·CH ₃ CN	
Ag1…Ag2	3.2413(14)	Ag…Ag′	3.2206(4)
Ag1…Ag3	3.2360(14)	Ag–As′	2.4746(3)
Ag1…Ag4	3.2264(14)	Ag–N1	2.347(2)
Ag1…Ag5	3.3016(14)	Ag–N2	2.361(2)
Ag1–As1	2.5780(15)	Ag–N3	2.371(3)
Ag1–As2	2.5869(16)	Symmetry code: (′) 1–x, 2–y, 1–z.	
Ag1–As3	2.5900(16)		
Ag1–As4	2.6041(15)		
Ag–N	2.260(13)–2.343(11)		

Complex **2** consists of two CuBr units bridged by two Py₃As ligands (μ_2 -As,N,N′) in a head-to-tail manner so that an inversion center is located in the middle of the molecule (Figure 2). Therefore, each Cu atom adopts a distorted tetrahedral [Cu@AsN₂Br] environment ($\tau_4 = 0.90$). The intramolecular Cu…Cu distances (*ca.* 3.94 Å) are too long for the appearance of metallophilic interactions (*cf.* twice van der Waals radius of Cu is 2.80 Å [51]). The dihedral angle between planes of the coordinated pyridine rings of **2** is about 124.8°. Overall, the structure of **2** closely resembles that of similar Py₃P-based complex [Cu₂(Py₃P)₂Br₂] [48].

Crystals of **3**·3H₂O contain three independent [Ag@Ag₄(Py₃As)₄]⁵⁺ cations charge-balanced by non-coordinated ClO₄[−] anions, as well as the lattice water molecules. The

independent $[\text{Ag}@\text{Ag}_4(\text{Py}_3\text{As})_4]^{5+}$ cations have a similar structure, which consists of a C_3 -symmetrical $\text{Ag}@\text{Ag}_4$ tetrahedral kernel supported by four Py_3As ligands. The central Ag atom adopts a slightly distorted tetrahedral geometry ($\tau_4 = 0.98$) constituted of four As atoms. Each vertex Ag atom of the $\text{Ag}@\text{Ag}_4$ kernel is coordinated by three N atoms of three neighboring Py_3As ligands, thus accepting a trigonal pyramidal geometry [3 + 1]. Considering that the average distance between central and vertex Ag atoms of $\text{Ag}@\text{Ag}_4$ kernel (3.25 Å) is shorter than twice van der Waals Ag radius (3.44 Å) [51], argentophilic interactions could occur (*vide infra*). To sum up, Py_3As ligands in **3** exhibit an As,N,N',N''-coordination manner that is similar to that of Py_3P in $[\text{Ag}@\text{Ag}_4(\text{Py}_3\text{P})_4]^{5+}$ complexes [52].

The structure of the cationic part of **4**· CH_3CN , $[\text{Ag}_2(\text{Py}_2\text{PhAs})_2(\text{MeCN})_2]^{2+}$, is formed by two Ag(I) cations bridged by two Py_2AsPh ligands in a head-to-tail manner. Both metal cations are also ligated by MeCN, thereby adopting a distorted trigonal pyramidal geometry. Again, the Ag... Ag distance in **4** being 3.2206(4) Å implies argentophilic interaction, which is actually taking place according to the theoretical calculations (*vide infra*).

The synthesized compounds are moderately soluble in dichloromethane and acetonitrile (**1**· CH_2Cl_2 and **2**), or in water (**3**· $3\text{H}_2\text{O}$ and **4**· CH_3CN). All of them are air-stable, except for **4**· CH_3CN , which quickly loses the coordinated acetonitrile molecules upon storage in air. The ^1H NMR spectra of **1–4** demonstrate one set of signals from the coordinated arsines and ancillary ligands (Figures S3–S7), indicating the existence of symmetrical species in a solution (closely uninvestigated). The mid-IR spectra of these complexes show characteristic bands of the coordinated pyridyl-containing arsenic ligands (Figure S8). Moreover, complexes **3**· $3\text{H}_2\text{O}$ and **4**· CH_3CN display a broad band at 1097–1099 cm^{-1} belonged of $\nu_{\text{Cl-O}}$ stretching vibrations of free ClO_4^- anions, and specific bands from H_2O and MeCN molecules/ligands, respectively, i.e., $\nu_{\text{O-H}} = 3610 \text{ cm}^{-1}$ and $\nu_{\text{C}\equiv\text{N}} = 2268 \text{ cm}^{-1}$.

The thermal stability of the above complexes has been studied by TGA, DTG and DTA techniques under argon atmosphere (Figure S9). The solvate molecules of **1**· CH_2Cl_2 are lost at the range of 100–127 °C, but complex **1** itself is stable up to ≈ 200 °C. A higher stability is inherent in **2**, which begins to decompose at about 240 °C. Compounds **3**· $3\text{H}_2\text{O}$ and **4**· CH_3CN lose the solvate molecules at 120–140 °C and 135–155 °C, respectively, after which they remain stable at least up to 270 °C.

2.2. Theoretical Consideration

The electronic structure of luminescent Cu(I) complexes **1** and **2** has been investigated at the PBE0/def2TZVP level of the theory (for details, see §6 in ESI) to understand electronic transitions responsible for the excitation. For both complexes, the highest occupied molecular orbital (HOMO) and nearby HOMO-n are largely contributed by metal' d-orbitals and the lone pairs in halogen atoms (Figure 3, Figures S11, S12; Tables S2, S3). The lowest unoccupied molecular orbital (LUMO) and nearby LUMO+n are mainly π -orbitals on the pyridine rings (Figure 3, Figures S11, S12; Tables S2, S3). Interestingly, a lone pair in As atom does not contribute to the highest MOs (HOMO–HOMO-6). The fact that the frontier MOs of **1** and **2** are well separated in the space indicates a quite small energy gap between the lowest singlet (S_1) and triplet (T_1) excited states. Overall, the predicted HOMO/LUMO distribution is very typical for emitting TADF Cu(I) halide complexes.

A detailed consideration of HOMOs of **1** and **2** reveals small energy gaps separation between the HOMO and HOMO-1 levels which are, moreover, populated by d-orbitals with different spatial orientations (Figures S11 and S12). In particular, the HOMO-1/HOMO separation is 140 cm^{-1} for **2**, and it is just 2 cm^{-1} for **1**. According to the literature [12,13], such a scenario demonstrates a strong SOC mixing of the S_1 and T_1 states, which are originated from HOMO-1 \rightarrow LUMO and HOMO \rightarrow LUMO transitions, respectively. This, in turn, accelerates the rates of both $S_1 \rightarrow T_1$ and $T_1 \rightarrow S_1$ spin-forbidden processes, and hence, increases total rate of the luminescence. The experimental results fully confirm these predictions (*vide infra*). TD-DFT computations of **1** and **2** testify to the (M + X) LCT character (X = Br or I) of the low-energy absorptions (Tables S4, S5) that is specific for the related complexes. Furthermore, the (M + X) LCT nature of the lowest excited states is

confirmed by a specific spin distribution in the computed T_1 state of **1** (Figure S15). The lowest (LSOMO) and highest (HSOMO) single occupied molecular orbitals of the T_1 state of **1** (Figure S15) closely resemble HOMO and LUMO in its S_0 state (Figure 3). The calculated $\Delta E(T_1-S_0)$ energy gap for the optimized states of **1** being 1.81 eV reasonably agrees with the emission energy of **1**·CH₂Cl₂ at a pure phosphorescence regime (77 K), i.e., 1.98 eV or 625 nm (*vide infra*). Therefore, one can expect that the emitting excited states of the compounds discussed should be of the (M + X) LCT type.

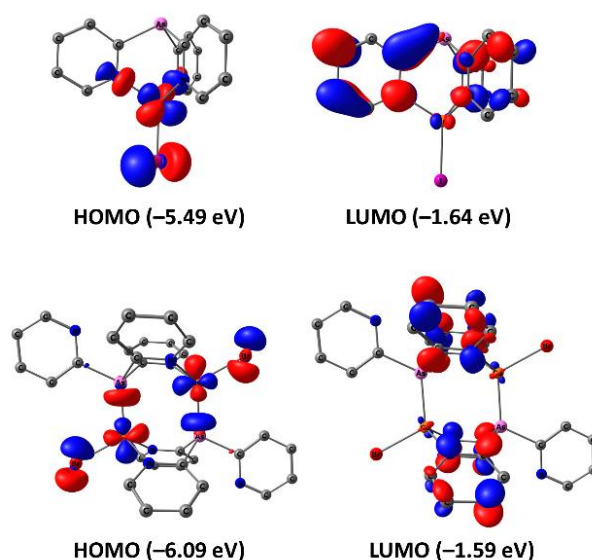


Figure 3. Frontier orbitals of **1** and **2** calculated at PBE0/def2TZVP level (isosurface = 0.045).

For Ag(I) complexes **3** and **4**, which appear to be almost non-emissive, argentophilic interactions have been examined by QTAIM (quantum theory “atoms in molecule”) method at the ω B97XD/DZP-DKH level (for details, see §6.3 in ESI). The QTAIM analysis of model structures reveals the presence of the bond critical points (3, -1) for metalophilic interactions in **3** and **4** (Table 2). The low magnitude of the electron density (0.017–0.021 a.u.), positive values of the Laplacian of electron density (0.028–0.030 a.u.), and negative energy density (from -0.002 to -0.003 a.u.) in the bond critical points (3, -1) for Ag(I)···Ag(I) interactions in **3** and **4** are typical for metalophilic interactions in other metal complexes [53–59]. The balance between the Lagrangian kinetic energy $G(\mathbf{r})$ and potential energy density $V(\mathbf{r})$ at the bond critical points (3, -1) for Ag(I)···Ag(I) interactions in **3** and **4** [*viz.* $-G(\mathbf{r})/V(\mathbf{r}) < 1$] shows some covalent contribution in these short contacts [60]. The Laplacian of electron density is typically decomposed into the sum of contributions along the three principal axes of maximal variation, giving three eigenvalues of the Hessian matrix (λ_1 , λ_2 and λ_3), and the sign of λ_2 can be utilized to distinguish the bonding (attractive, $\lambda_2 < 0$) weak interactions from the non-bonding ones (repulsive, $\lambda_2 > 0$) [61,62]. Thus, the Ag(I)···Ag(I) interactions in **3** and **4** have an attractive character. For illustration, the calculated electron density distribution at the metal atoms of **4** is plotted in Figure 4.

Table 2. Values of the density of all electrons $\rho(\mathbf{r})$, Laplacian of electron density $-\nabla^2\rho(\mathbf{r})$ and appropriate λ_2 eigenvalues, energy density $-H_b$, potential energy density $-V(\mathbf{r})$, Lagrangian kinetic energy $-G(\mathbf{r})$, and electron localization function – ELF at the bond critical points (3, -1), corresponding to Ag(I)⋯Ag(I) interactions in **3** and **4**.

Ag⋯Ag Contact	$\rho(\mathbf{r})$	$\nabla^2\rho(\mathbf{r})$	λ_2	H_b	$V(\mathbf{r})$	$G(\mathbf{r})$	ELF
Complex 3							
3.241 Å	0.019 a.u.	0.030 a.u.	−0.019 a.u.	−0.003 a.u.	−0.013 a.u.	0.010 a.u.	0.125 a.u.
3.236 Å	0.019 a.u.	0.029 a.u.	−0.019 a.u.	−0.003 a.u.	−0.013 a.u.	0.010 a.u.	0.129 a.u.
3.226 Å	0.020 a.u.	0.030 a.u.	−0.020 a.u.	−0.003 a.u.	−0.014 a.u.	0.011 a.u.	0.129 a.u.
3.302 Å	0.017 a.u.	0.029 a.u.	−0.017 a.u.	−0.003 a.u.	−0.012 a.u.	0.009 a.u.	0.112 a.u.
3.249 Å	0.019 a.u.	0.029 a.u.	−0.019 a.u.	−0.003 a.u.	−0.013 a.u.	0.010 a.u.	0.124 a.u.
3.252 Å	0.019 a.u.	0.029 a.u.	−0.019 a.u.	−0.003 a.u.	−0.013 a.u.	0.010 a.u.	0.124 a.u.
3.281 Å	0.018 a.u.	0.029 a.u.	−0.018 a.u.	−0.002 a.u.	−0.012 a.u.	0.010 a.u.	0.117 a.u.
3.209 Å	0.020 a.u.	0.030 a.u.	−0.020 a.u.	−0.003 a.u.	−0.014 a.u.	0.011 a.u.	0.136 a.u.
3.222 Å	0.020 a.u.	0.029 a.u.	−0.020 a.u.	−0.003 a.u.	−0.014 a.u.	0.011 a.u.	0.134 a.u.
3.214 Å	0.020 a.u.	0.030 a.u.	−0.020 a.u.	−0.003 a.u.	−0.014 a.u.	0.011 a.u.	0.134 a.u.
3.247 Å	0.019 a.u.	0.030 a.u.	−0.019 a.u.	−0.003 a.u.	−0.013 a.u.	0.010 a.u.	0.125 a.u.
3.313 Å	0.017 a.u.	0.029 a.u.	−0.017 a.u.	−0.002 a.u.	−0.011 a.u.	0.009 a.u.	0.110 a.u.
Complex 4							
3.221 Å	0.021 a.u.	0.028 a.u.	−0.021 a.u.	−0.003 a.u.	−0.014 a.u.	0.011 a.u.	0.156 a.u.

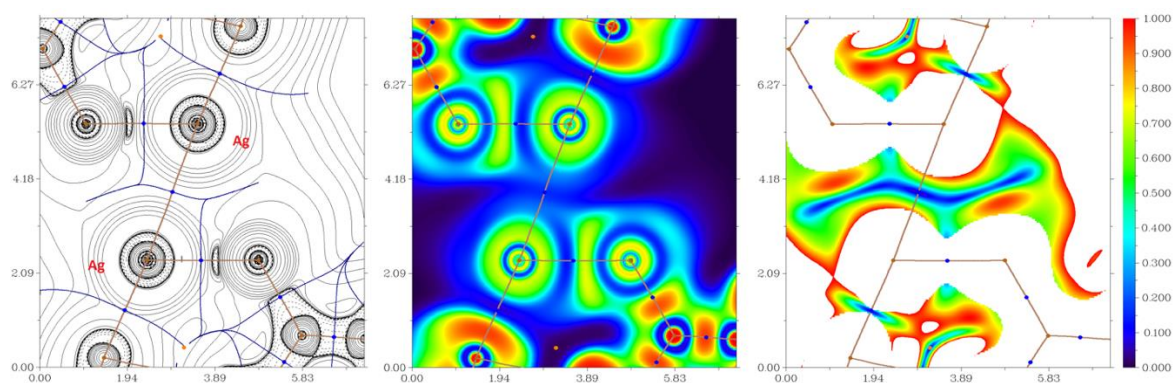


Figure 4. Contour line diagram of the Laplacian of electron density distribution $\nabla^2\rho(\mathbf{r})$, bond paths, and selected zero-flux surfaces (left panel), visualization of electron localization function (ELF, center panel) and reduced density gradient (RDG, right panel) analyses for metalphilic interactions in complex **4**. Bond critical points (3, -1) are shown in blue, nuclear critical points (3, -3)—in pale brown, ring critical points (3, $+1$)—in orange, bond paths are shown as pale brown lines, length units – Å, and the color scale for the ELF and RDG maps is presented in a.u.

2.3. Photoluminescence of **1** and **2**

At ambient temperature, Cu(I) complexes **1**, **1a** and **2** emit pronounced solid state photoluminescence (PL), whereas Ag(I) derivatives **3** and **4** appear to be almost non-emissive. The recorded emission and excitation spectra of **1**, **1a** and **2** are shown in Figure 5, and the measured PL properties are given in Table 3. As follows from these data, scorpionate **1** manifests an orange PL, while dimers **1a** and **2** emit in a green region. In the terms of PL quantum yields (PLQYs), the emission of the studied compounds is moderate at 298 K (10–14%). All the emission profiles are of broad and structureless shape that is inherent in

PL of the charge transfer origin [14]. The corresponding excitation curves are displayed by typical bands extending from the UV-edge and are sharply falling close at ≈ 450 nm (**1a**, **2**) or 590 nm (**1**). The fact that the emission and emission profiles of iodide **1a** and bromide **2** are almost superimposable is not confusing; previously, the similar cases were documented for other halide complexes, including the related ones [38,48,63]. The PL lifetimes of **1**, **1a** and **2** at 298 K are remarkably short (0.8–1.9 μs) compared to the most known Cu(I) complexes. Accordingly, the radiative constants ($k_r = \text{PLQY}/\tau$) being $(0.53\text{--}1.75)\cdot 10^5 \text{ s}^{-1}$ are relatively high, thereby indicating a strong SOC effect that is also predicted by DFT calculations (*vide supra*). For comparison, radiative rates (k_r) of the similar Py_3P -based complexes $[\text{Cu}_2(\text{Py}_3\text{P})_2\text{X}_2]$ at 298 K are much lower: $2.9\cdot 10^4$ and $2.6\cdot 10^4 \text{ s}^{-1}$ for X = Br and I, respectively. The acceleration of the emission rates observed in the arsine complexes is obviously attributed to much stronger SOC effect of arsenic compared to that of phosphorus. Previously, this effect was already demonstrated for Cu(I)-arsine complexes [38].

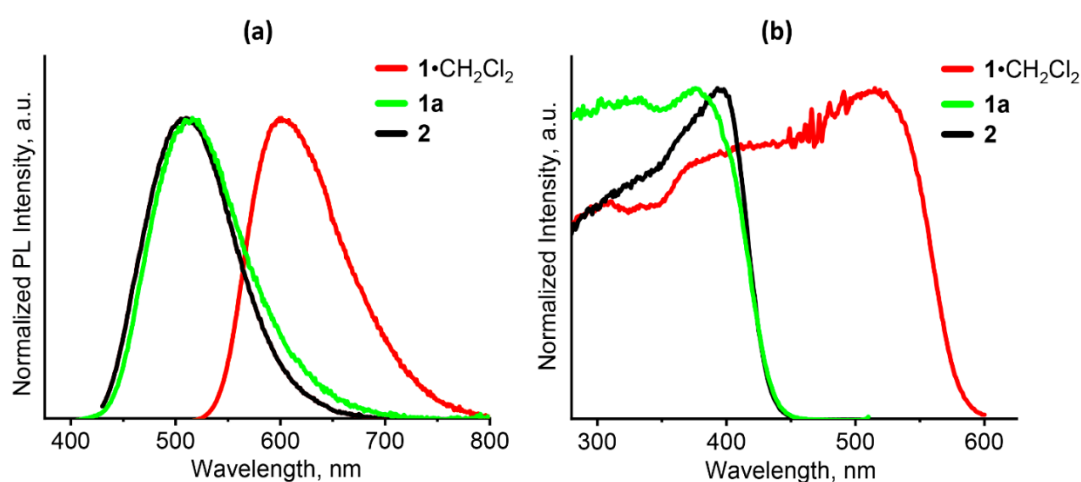


Figure 5. Emission (a) and excitation (b) spectra of **1**· CH_2Cl_2 , **2** and **3**· $3\text{H}_2\text{O}$ at 300 K. The emission spectra were recorded at $\lambda_{\text{ex}} = 390$ nm (for **1a**, **2**) and 500 nm (**1**· CH_2Cl_2).

Table 3. Luminescent characteristics of Cu(I) complexes **1**, **1a** and **2**.

Complex	λ_{em} , nm		PL Lifetime, μs		PLQY, % [298 K]
	298 K	77 K	298 K	77 K	
1 · CH_2Cl_2	605	625	1.9	25	10 ^a
1a	511	-	0.8	-	14 ^b
2	510	520	0.9	23	12 ^b

^a $\lambda_{\text{ex}} = 500$ nm, ^b $\lambda_{\text{ex}} = 390$ nm.

Temperature-dependent PL spectra of **1** and **2** (Figure 6) demonstrate the significant enhancement of PL intensity upon cooling that is accompanied by a slight bathochromic shift of the bands by 10–20 nm (Table 3). When passing from 298 to 77 K, the PL lifetimes of **1** and **2** increase by 13 and 25 times, thus amounting 25 and 23 μs at 77 K, respectively. Taken together, these observations suggest the TADF manifestation at ambient temperature and phosphorescence at 77 K. According to the DFT and TD-DFT computations, the $^1(\text{M} + \text{X})$ LCT emissive state is responsible for TADF (298 K), and $^3(\text{M} + \text{X})$ LCT state is active at the phosphorescence regime (77 K). It should be underlined that the same emission scheme was previously proved for the related dimeric complexes based on Py_3P and PhPy_2As ligands. The ΔE_{ST} energy gaps between the $^1(\text{M} + \text{X})$ LCT and $^3(\text{M} + \text{X})$ LCT states of **1** and **2** can be roughly estimated by the red-shifting of the left flank of emission bands at their half height (Figure S17). The estimated ΔE_{ST} gaps, being 340 and 890 cm^{-1} for **1** and **2**, respectively, fall close to the range of such values ($\Delta E_{\text{ST}} < 1500 \text{ cm}^{-1}$) for TADF-active Cu(I) complexes [12–14].

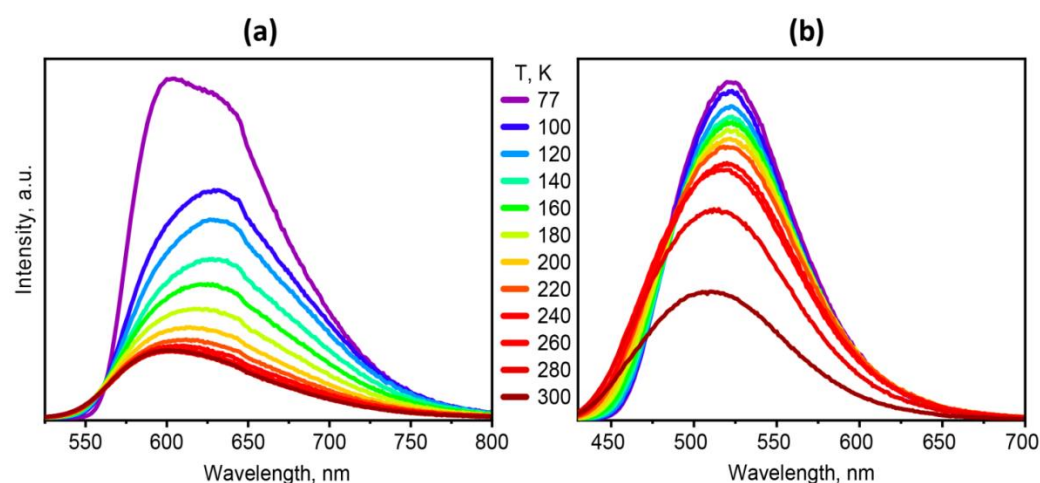


Figure 6. Temperature dependent emission spectra of **1**·CH₂Cl₂ (a) and **2** (b) recorded at $\lambda_{\text{ex}} = 500$ and 380 nm, respectively.

3. Materials and Methods

3.1. General

All synthetic procedures were carried out under an argon atmosphere using the standard Schlenk technique. CuI ($\geq 99\%$, Sigma, Gillingham, UK), AgClO₄ (97%, Alfa Aesar, Heysham, UK), and MeCN (HPLC grade, Cryochrom, St. Petersburg, Russia) were used as purchased. Prior to use, CuBr was freshly synthesized by the treatment of CuBr₂ with Cu powder in MeCN solution. Tris(2-pyridyl)arsine, [50] and bis(2-pyridyl)phenylarsine (Py₂AsPh) [38] were prepared according to the literature procedures. ¹H NMR spectra were recorded using a Bruker AV-500 spectrometer at 500.13 MHz. Chemical shifts were reported in δ (ppm) relative to residual peaks of protonated CDCl₃, DMSO-d₆, and CD₃CN. FT-IR spectra were recorded on a Bruker Vertex 80 spectrometer. Powder X-ray diffraction patterns were recorded on a Shimadzu XRD-7000 diffractometer (Cu-K α radiation, Ni – filter, 3–35° 2 θ range, 0.03° 2 θ step, 5s per point). Thermogravimetric analyses (TGA – c-DTA – DTG) were carried out in a closed Al₂O₃ pan under argon flow at a 10 °C/min⁻¹ heating rate using a NETZSCH STA 449 F1 Jupiter STA. CHN microanalyses were performed on a MICRO cube analyzer.

Emission and excitation spectra were recorded on a Fluorolog 3 spectrometer (Horiba Jobin Yvon) equipped with a cooled PC177CE-010 photon detection module and an R2658 photomultiplier. The absolute PLQYs were determined at 298 K using a Fluorolog 3 Quanta-phi integrating sphere. Temperature-dependent excitation and emission spectra as well as emission decays were recorded using an Optistat DN optical cryostat (Oxford Instruments) integrated with the above spectrometer.

3.2. [Cu(Py₃As)I]·CH₂Cl₂ (**1**·CH₂Cl₂)

A mixture of CuI (16.5 mg, 0.087 mmol) and Py₃As (30 mg, 0.097 mmol) in CH₂Cl₂ (2 mL) was stirred at room temperature for 10 min. To the resulting solution, hexane (1 mL) was added dropwise and a precipitate formed was centrifuged and dried in air. Orange powder. Yield: 39 mg (89%). Single crystals of **1**·CH₂Cl₂ were grown by slow evaporation of CH₂Cl₂ solution for overnight. ¹H NMR (500.13 MHz, CDCl₃, ppm), δ : 9.09 (ddd, $J = 5.0$ Hz, $J = 1.9$ Hz, $J = 0.9$ Hz, 3H, H⁶ in Py), 7.90 (dt, $J = 7.5$ Hz, $J = 1.2$ Hz, 3H, H⁴ in Py), 7.71 (dt, $J = 7.6$ Hz, $J = 1.8$ Hz, 3H, H⁵ in Py), 7.35 (ddd, $J = 7.7$ Hz, $J = 5.0$ Hz, $J = 1.3$ Hz, 3H, H³ in Py), 5.31 (s, 2H in CH₂Cl₂). FT-IR (KBr, cm⁻¹): 409 (m), 457 (w), 482 (s), 617 (w), 638 (w), 669 (w), 702 (m), 733 (s), 758 (vs), 773 (m), 787 (m), 897 (vw), 1003 (m), 1045 (m), 1088 (w), 1103 (w), 1152 (m), 1227 (w), 1271 (m), 1422 (s), 1447 (vs), 1553 (m), 1572 (s), 1636 (vw), 2955 (w), 3028 (w), 3042 (w). Calculated for C₁₆H₁₄AsCuI₂N₃ (584.58): C, 32.9; H, 2.4; N, 7.2. Found: C, 33.0; H, 2.5; N, 7.2.

3.3. $[Cu_2(Py_3As)_2I_2]$ (**1a**)

Method 1: A solid sample of **1**·CH₂Cl₂ (15 mg, 0.026 mmol) was placed in a 3 mL vial, which was then placed in a closed 50 mL weighing bottle containing MeCN (≈0.5 mL) on a bottom. Exposure of a solid sample **1**·CH₂Cl₂ under MeCN vapor at ambient temperature for 1 h results in the formation of **1a** as an off-white solid. Yield: 99% (12.5 mg).

Method 2: A mixture of CuI (8.5 mg, 0.045 mmol) and Py₃As (15 mg, 0.049 mmol) in CH₃CN (1 mL) was stirred at room temperature for 10 min. The formed precipitate was centrifuged and dried in vacuum. White powder. Yield: 40 mg (89%).

¹H NMR (500.13 MHz, CD₃CN, ppm), δ: 8.88 (d, *J* = 5.0 Hz, 6H, H⁶ in Py), 8.03 (d, *J* = 7.6 Hz, 6H, H⁴ in Py), 7.85 (t, *J* = 7.7 Hz, 6H, H⁵ in Py), 7.49–7.43 (m, 6H, H³ in Py). FT-IR (KBr, cm⁻¹): 405 (w), 419 (m), 459 (w), 474 (m), 484 (s), 617 (w), 637 (m), 741 (w), 756 (vs), 779 (m), 988 (m), 1007 (m), 1049 (m), 1088 (w), 1103 (w), 1119 (w), 1155 (m), 1227 (w), 1275 (m), 1410 (s), 1423 (vs), 1447 (vs), 1558 (s), 1570 (s), 1578 (s), 1634 (w), 2974 (m), 3038 (m), 3059 (m). Calculated for C₃₀H₂₄As₂Cu₂I₂N₆ (999.29): C, 36.1; H, 2.4; N, 8.4. Found: C, 36.0; H, 2.4; N, 8.3.

3.4. $[Cu_2(Py_3As)_2Br_2]$ (**2**)

A mixture of CuBr (12 mg, 0.083 mmol) and Py₃As (26 mg, 0.084 mmol) in CH₃CN (1 mL) was stirred at room temperature for 10 min. The formed precipitate was centrifuged and dried in vacuum. White powder. Yield: 69 mg (92%). Single crystals of **2** were grown by a diffusion of Et₂O vapor into an CH₃CN solution for overnight. ¹H NMR (500.13 MHz, CDCl₃, ppm), δ: 9.07 (d, *J* = 4.8 Hz, 6H, H⁶ in Py), 7.92–7.86 (m, 6H, H⁴ in Py), 7.71 (t, *J* = 7.9 Hz, 6H, H⁵ in Py), 7.38–7.32 (m, 6H, H³ in Py). FT-IR (KBr, cm⁻¹): 405 (m), 417 (m), 459 (w), 474 (m), 490 (s), 619 (w), 637 (m), 671 (w), 696 (w), 733 (w), 743 (w), 766 (vs), 775 (vs), 889 (vw), 966 (w), 989 (m), 1007 (m), 1045 (m), 1082 (w), 1105 (w), 1121 (w), 1153 (m), 1233 (vw), 1277 (w), 1414 (s), 1427 (s), 1449 (vs), 1558 (m), 1578 (s), 1638 (vw), 2953 (w), 2978 (w), 3032 (m), 3057 (w). Calculated for C₃₀H₂₄As₂Cu₂Br₂N₆ (905.29): C, 39.8; H, 2.7; N, 9.3. Found: C, 39.7; H, 2.8; N, 9.3.

3.5. $[Ag@Ag_4(Py_3As)_4](ClO_4)_5 \cdot 3H_2O$ (**3**·3H₂O)

A mixture of AgClO₄ (20.5 mg, 0.099 mmol) and Py₃As (25 mg, 0.081 mmol) in CH₃CN (1 mL) was stirred at room temperature for 10 min. To the resulting solution, diethyl ether (1 mL) was then added, and the precipitate formed was centrifuged and dried in vacuum. White powder. Yield: 156 mg (83%). Single crystals of **3**·3H₂O were grown by slow evaporation of water solution for few days. ¹H NMR (500.13 MHz, CD₃CN, ppm), δ: 8.27–8.21 (m, 12H, H⁶ in Py), 7.89 (t, *J* = 7.6 Hz, 12H, H⁴ in Py), 7.40 (t, *J* = 6.5 Hz, 12H, H⁵ in Py), 7.02 (d, *J* = 7.8 Hz, 12H, H³ in Py). FT-IR (KBr, cm⁻¹): 405 (m), 467 (s), 507 (m), 621 (vs), 665 (m), 702 (m), 758 (s), 903 (m), 928 (m), 1005 (s), 1047 (vs), 1082 (vs), 1097 (vs), 1165 (m), 1246 (vw), 1287 (w), 1427 (s), 1452 (s), 1558 (m), 1578 (s), 1630 (w), 2995 (w), 3084 (m), 3610 (w). Calculated for C₆₀H₅₄As₄Ag₅N₁₂Cl₅O₂₃ (2327.43): C, 31.0; H, 2.3; N, 7.2. Found: C, 30.9; H, 2.5; N, 7.2.

3.6. $[Ag_2(Py_2AsPh)_2(MeCN)_2](ClO_4)_2 \cdot CH_3CN$ (**4**·CH₃CN)

A mixture of AgClO₄ (15 mg, 0.073 mmol) and bis(2-pyridyl)phenylarsine (25 mg, 0.081 mmol) in CH₃CN (1 mL) was stirred at room temperature for 10 min. To a resulting solution, diethyl ether (1 mL) was then added, and the precipitate formed was centrifuged and dried in vacuum. White powder. Yield: 72 mg (85%). Single crystals of **4**·CH₃CN were grown by a diffusion of Et₂O vapor into an CH₃CN solution for overnight. ¹H NMR (500.13 MHz, DMSO-d₆, ppm), δ: 8.73 (d, *J* = 5.0 Hz, 4H, H⁶ in Py), 7.87 (t, *J* = 7.8 Hz, 4H, H⁴ in Py), 7.56–7.46 (m, 14H, H⁵ in Py, *o*-H, *m*-H and *p*-H in Ph), 7.43 (d, *J* = 7.9 Hz, 4H, H³ in Py). FT-IR (KBr, cm⁻¹): 405 (w), 469 (m), 488 (m), 623 (s), 696 (m), 743 (s), 764 (m), 926 (w), 989 (m), 1001 (m), 1049 (s), 1099 (vs), 1161 (m), 1236 (vw), 1287 (w), 1425 (s), 1437 (m), 1454 (s), 1483 (w), 1560 (m), 1580 (m), 1636 (w), 1973 (vw), 2251 (w), 2268 (w), 3059 (w).

Calculated for $C_{38}H_{35}As_2Ag_2N_7Cl_2O_8$ (1154.21): C, 39.5; H, 3.1; N, 8.5. Found: C, 39.5; H, 3.0; N, 8.5.

3.7. X-ray Crystallography

The data were collected on a Bruker Kappa Apex II CCD diffractometer using φ , ω -scans of narrow (0.5°) frames with Mo $K\alpha$ radiation ($\lambda = 0.71073 \text{ \AA}$) and a graphite monochromator. The structures were solved by direct methods SHELXL97 and refined by a full matrix least-squares anisotropic-isotropic (for H atoms) procedure using the SHELXL-2018/3 programs set [64]. Absorption corrections were applied using the empirical multiscan method with the SADABS program [65]. The positions of the hydrogen atoms were calculated with the riding model. Free solvent accessible volume in compound **3** derived from PLATON routine analysis was found to be 8.5% (1001.0 \AA^3). This volume is occupied by H_2O molecules, but this structure is based on very weak data (a better dataset cannot be obtained). Therefore, we employed the PLATON/SQUEEZE procedure to calculate the contribution to the diffraction from H_2O molecules and thereby produced a set of H_2O -free diffraction intensities. The final formula of **3**, $C_{60}H_{48}Ag_5As_4N_{12}Cl_5O_{10}$, was derived from the SQUEEZE results. The crystallographic data and details of the structure refinements are summarized in Table S1.

CCDC 2090740, 2090741, 2126017 and 2126016 contain the supplementary crystallographic data for this paper. These data can be obtained free of charge from The Cambridge Crystallographic Data Center at <https://www.ccdc.cam.ac.uk/structures/> (accessed on 1 July 2022).

4. Conclusions

In conclusion, the reactions of tris(2-pyridyl)arsine (Py_3As), an earlier unexplored ligand, with CuI, CuBr, and $AgClO_4$ have been studied. The interaction with CuI features a remarkable solvent-directing effect on the product structure. This reaction in CH_2Cl_2 results in the crystallization of mononuclear scorpionate $[Cu(Py_3As)I] \cdot CH_2Cl_2$, whilst MeCN favors the selective formation of the dimer $[Cu_2(Py_3As)_2I_2]$. Noteworthy, scorpionate $[Cu(Py_3As)I] \cdot CH_2Cl_2$, when fumed with MeCN vapor, easily (r.t., 1 h) and quantitatively dimerizes into $[Cu_2(Py_3As)_2I_2]$. On the contrary, the treatment of Py_3As with CuBr, regardless of solvent nature, affords the dimer $[Cu_2(Py_3As)_2Br_2]$ only. At ambient temperature, the above Cu(I) complexes manifest visible photoluminescence with noticeably short decay times (0.8–1.9 μs) and moderate quantum yields (10–14%). Taking into account the results of DFT computations and temperature-dependent photophysical measurements, the emission observed has been tentatively assigned to the thermally activated delayed fluorescence of (M + X) LCT kind (M = Cu, L = Py_3As ; X = halogen).

Complexation of Py_3As with $AgClO_4$ results in the assembly of complex $[Ag@Ag_4(Py_3As)_4](ClO_4)_5$, containing Ag-centered tetrahedron $Ag@Ag_4$ supported by four Py_3As ligands. According to QTAIM analysis of this cluster, argentophilic interactions between its central and peripheral Ag(I) cations are observed.

To sum up, our findings reveal that the coordination chemistry of Py_3As in some cases, e.g., in the reactions with Cu halides, may differ from that of Py_3P . Moreover, the Py_3As -derived Cu(I) complexes demonstrate higher emission rates (k_r) at 298 K compared to the similar Py_3P -based analogs, thus highlighting the prospects of employing the arsine ligands for the design of short-lived TADF materials.

Supplementary Materials: The following supporting information can be downloaded at: <https://www.mdpi.com/article/10.3390/molecules27186059/s1>, Table S1. X-ray crystallographic data for **1**· CH_2Cl_2 , **2**, **3**· $3H_2O$ and **4**· CH_3CN ; Figure S1. Experimental and simulated PXRD patterns of an as-synthesized sample of **1**· CH_2Cl_2 ; Figure S2. Experimental and simulated PXRD patterns of an as-synthesized sample of **2**; Figure S3. 1H NMR spectrum of **1**· CH_2Cl_2 ($CDCl_3$, 25 °C); Figure S4. 1H NMR spectrum of **1a** (CD_3CN , 25 °C); Figure S5. 1H NMR spectrum of **2** ($CDCl_3$, 25 °C); Figure S6. 1H NMR spectrum of **3**· $3H_2O$ (CD_3CN , 25 °C); Figure S7. 1H NMR spectrum of **4**· CH_3CN ($DMSO-d_6$, 25 °C); Figure S8. FT-IR spectra for the complexes **1**· CH_2Cl_2 , **1a**, **2**, **3**· $3H_2O$ and **4**· CH_3CN

in the 400–3250 cm^{-1} region; Figure S9. TGA&DTG curves for **1**·CH₂Cl₂, **2**, **3**·3H₂O and **4**·CH₃CN; Figure S10. Gibbs free energies calculated for the equilibria $2 [\text{Cu}(\text{Py}_3\text{As})\text{X}] \leftrightarrow [\text{Cu}_2(\text{Py}_3\text{As})_2\text{X}_2]$ (X = Br, I) at PBE0/def2TZVP level; Figure S11. Selected frontier molecular orbitals (isovalue = 0.04) calculated for the optimized S₀ state geometry of [Cu(AsPy₃)I] (**1**) at PBE0/def2TZVP level; Figure S12. Selected frontier molecular orbitals (isovalue = 0.04) calculated for the optimized S₀ state geometry of [Cu₂(Py₃As)₂Br₂] (**2**) at PBE0/def2TZVP level; Figure S13. The UV-Vis spectrum of [Cu(AsPy₃)I] (**1**) (CH₂Cl₂, 298 K) and absorption patterns (vertical bars) calculated at the TD-PBE0/def2TZVP level; Figure S14. The UV-Vis spectrum of [Cu₂(Py₃As)₂Br₂] (**2**) (MeCN, 298 K) and absorption patterns (vertical bars) calculated at the TD-PBE0/def2TZVP level; Table S2. Atomic contributions to selected molecular orbitals of [Cu(AsPy₃)I] (**1**) in the ground state (S₀) geometry according Mulliken population analysis at PBE0/def2TZVP level; Table S3. Atomic contributions to selected molecular orbitals of [Cu₂(Py₃As)₂Br₂] (**2**) in the ground state (S₀) geometry according Mulliken population analysis at PBE0/def2TZVP level; Table S4. Calculated (TD-PBE0/def2-TZVP) energies and characters of the main singlet excitations ($f > 0.01$) of [Cu(AsPy₃)I] (**1**); Table S5. Calculated (TD-PBE0/def2-TZVP) energies and characters of the main singlet excitations ($f > 0.01$) of [Cu₂(Py₃As)₂Br₂] (**2**); Figure S15. LSOMO and HSOMO (isovalue = 0.04) calculated for the optimized gas phase T₁ state geometry of [Cu(AsPy₃)I] (**1**) at PBE0/def2TZVP level; Figure S16. Temperature dependent excitation spectra of **1**·CH₂Cl₂ (a) and **2** (b) recorded at $\lambda_{\text{reg}} = 595$ and 520 nm, respectively; Figure S17. Red-shifting emission profile of **1**·CH₂Cl₂ (left) and **2** (right) upon cooling from 298 to 77 K; Figure S18. PL decay kinetics for **1**·CH₂Cl₂ (left) and **2** (right). Citation of reference [66–78].

Author Contributions: Investigation data curation, visualization, Y.V.D.; Photophysical measurements, M.I.R.; DFT calculations, E.H.S. and A.S.N.; Crystallography, I.Y.B.; Project conceptualization, administration, supervision, writing-review and editing, and funding acquisition, A.V.A. All authors have read and agreed to the published version of the manuscript.

Funding: This work was supported by Russian Science Foundation (Project No. 21-73-10110) and the Ministry of Science and Higher Education of the Russian Federation (projects No. 121031700321-3, No. 121031700313-8, and No. 1021051503141-0-1.4.1).

Institutional Review Board Statement: Not applicable.

Informed Consent Statement: Not applicable.

Acknowledgments: The DFT calculations and topological analysis of the electron density distribution were supported by the RUDN University Strategic Academic Leadership Program. We thank Andrey Baranov (Nikolaev Institute of Inorganic Chemistry) for help in synthesis of **1**. The authors would like to acknowledge the Multi-Access Chemical Research Center SB RAS for spectral and analytical measurements.

Conflicts of Interest: The authors declare no conflict of interest.

Sample Availability: Samples used are available from the authors. Crystallographic details, ¹H NMR and FT-IR spectra, TGA&DTG curves, and computation details.

References

1. Lescop, C. Coordination-Driven Supramolecular Synthesis Based on Bimetallic Cu(I) Precursors: Adaptive Behavior and Luminescence. *Chem. Rec.* **2020**, *21*, 544–557. [[CrossRef](#)] [[PubMed](#)]
2. Marchenko, R.D.; Sukhikh, T.S.; Ryadun, A.A.; Potapov, A.S. Synthesis, Crystal Structure, and Luminescence of Cadmium(II) and Silver(I) Coordination Polymers Based on 1,3-Bis(1,2,4-triazol-1-yl)adamantane. *Molecules* **2021**, *26*, 5400. [[CrossRef](#)] [[PubMed](#)]
3. Moutier, F.; Schiller, J.; Calvez, G.; Lescop, C. Self-assembled luminescent Cu(I) tetranuclear metallacycles based on 3,3'-bipyridine ligands. *Org. Chem. Front.* **2021**, *8*, 2893–2902. [[CrossRef](#)]
4. Marchenko, R.D.; Lysova, A.A.; Samsonenko, D.G.; Dybtsev, D.N.; Potapov, A.S. Synthesis, structural diversity, luminescent properties and antibacterial effects of cadmium(II) and silver(I) coordination compounds with bis(1,2,3-benzotriazol-1-yl)alkanes. *Polyhedron* **2020**, *177*, 114330. [[CrossRef](#)]
5. Khisamov, R.; Sukhikh, T.; Bashirov, D.; Ryadun, A.; Konchenko, S. Structural and Photophysical Properties of 2,1,3-Benzothiadiazole-Based Phosph(III)azane and Its Complexes. *Molecules* **2020**, *25*, 2428. [[CrossRef](#)]
6. Sukhikh, T.S.; Khisamov, R.M.; Konchenko, S.N. Unexpectedly Long Lifetime of the Excited State of Benzothiadiazole Derivative and Its Adducts with Lewis Acids. *Molecules* **2021**, *26*, 2030. [[CrossRef](#)]
7. Abramov, P.A.; Komarov, V.Y.; Pischur, D.A.; Sulyaeva, V.S.; Benassi, E.; Sokolov, M.N. Solvatomorphs of (Bu₄N)₂[(Ag(N₂-py))₂Mo₈O₂₆]: Structure, colouration and phase transition. *CrystEngComm* **2021**, *23*, 8527–8537. [[CrossRef](#)]

8. Chupina, A.V.; Shayapov, V.; Novikov, A.S.; Volchek, V.V.; Benassi, E.; Abramov, P.A.; Sokolov, M.N. $[\{AgL\}_2Mo_8O_{26}]^{n-}$ complexes: A combined experimental and theoretical study. *Dalton Trans.* **2020**, *49*, 1522–1530. [[CrossRef](#)]
9. Chupina, A.V.; Mukhacheva, A.A.; Abramov, P.A.; Sokolov, M.N. Complexation and Isomerization of $[\beta-Mo_8O_{26}]^{4-}$ in the Presence of Ag^+ and DMF. *J. Struct. Chem.* **2020**, *61*, 299–308. [[CrossRef](#)]
10. Shmakova, A.A.; Berezin, A.S.; Abramov, P.A.; Sokolov, M.N. Self-Assembly of $Ag^+/[PW_{11}NbO_{40}]^{4-}$ Complexes in Nonaqueous Solutions. *Inorg. Chem.* **2020**, *59*, 1853–1862. [[CrossRef](#)]
11. Li, J.-J.; Liu, C.-Y.; Guan, Z.-J.; Lei, Z.; Wang, Q.-M. Anion-Directed Regulation of Structures and Luminescence of Heterometallic Clusters. *Angew. Chem. Int.* **2022**, *61*, e202201549.
12. Leitzl, M.J.; Zink, D.M.; Schinabeck, A.; Baumann, T.; Volz, D.; Yersin, H. Copper(I) Complexes for Thermally Activated Delayed Fluorescence: From Photophysical to Device Properties. *Top. Curr. Chem.* **2016**, *374*, 141–174. [[CrossRef](#)]
13. Yersin, H.; Rausch, A.F.; Czerwieńiec, R.; Hofbeck, T.; Fischer, T. The triplet state of organo-transition metal compounds. Triplet harvesting and singlet harvesting for efficient OLEDs. *Coord. Chem. Rev.* **2011**, *255*, 2622–2652. [[CrossRef](#)]
14. Yersin, H.; Czerwieńiec, R.; Shafikov, M.Z.; Suleymanova, A.F. TADF Material Design: Photophysical Background and Case Studies Focusing on Cu^I and Ag^I Complexes. *ChemPhysChem* **2017**, *18*, 3508–3535. [[CrossRef](#)] [[PubMed](#)]
15. Zhu, K.; Cheng, Z.; Rangan, S.; Cotlet, M.; Du, J.; Kasaei, L.; Kasaei, L.; Teat, S.J.; Liu, W.; Chen, Y.; et al. A New Type of Hybrid Copper Iodide as Nontoxic and Ultrastable LED Emissive Layer Material. *ACS Energy Lett.* **2021**, *6*, 2565–2574. [[CrossRef](#)]
16. Hei, X.; Liu, W.; Zhu, K.; Teat, S.J.; Jensen, S.; Li, M.; O'Carroll, D.M.; Wei, K.; Tan, K.; Cotlet, M.; et al. Blending Ionic and Coordinate Bonds in Hybrid Semiconductor Materials: A General Approach toward Robust and Solution-Processable Covalent/Coordinate Network Structures. *J. Am. Chem. Soc.* **2020**, *142*, 4242–4253. [[CrossRef](#)]
17. Vinogradova, K.A.; Plyusnin, V.F.; Kupryakov, A.S.; Rakhmanova, M.I.; Pervukhina, N.V.; Naumov, D.Y.; Sheludyakova, L.A.; Nikolaenkova, E.B.; Krivopalov, V.P.; Bushuev, M.B. Halide impact on emission of mononuclear copper(I) complexes with pyrazolylpyrimidine and triphenylphosphine. *Dalton Trans.* **2014**, *43*, 2953–2960. [[CrossRef](#)]
18. Shekhovtsov, N.A.; Kokina, T.E.; Vinogradova, K.A.; Panarin, A.Y.; Rakhmanova, M.I.; Naumov, D.Y.; Pervukhina, N.V.; Nikolaenkova, E.B.; Krivopalov, V.P.; Czerwieńiec, R.; et al. Near-infrared emitting copper(I) complexes with a pyrazolylpyrimidine ligand: Exploring relaxation pathways. *Dalton Trans.* **2022**, *51*, 2898–2911. [[CrossRef](#)] [[PubMed](#)]
19. Evariste, S.; El Sayed Moussa, M.; Wong, H.-L.; Calvez, G.; Yam, V.W.-W.; Lescop, C. Straightforward Preparation of a Solid-state Luminescent Cu_{11} Polymetallic Assembly via Adaptive Coordination-driven Supramolecular Chemistry. *Z. Anorg. Allg. Chem.* **2020**, *646*, 754–760. [[CrossRef](#)]
20. Shekhovtsov, N.A.; Vinogradova, K.A.; Berezin, A.S.; Sukhikh, T.S.; Krivopalov, V.P.; Nikolaenkova, E.B.; Bushuev, M.B. Excitation wavelength dependent emission of silver(I) complexes with a pyrimidine ligand. *Inorg. Chem. Front.* **2020**, *7*, 2212–2223. [[CrossRef](#)]
21. Malakhova, Y.A.; Sukhikh, T.S.; Rakhmanova, M.I.; Vinogradova, K.A. Effect of polymorphism on the luminescent properties on silver(I) nitrate complexes with 2-amino-5-phenylpyrazine. *J. Struct. Chem.* **2022**, *63*, 485–500. [[CrossRef](#)]
22. Dumur, F. Recent advances in organic light-emitting devices comprising copper complexes: A realistic approach for low-cost and highly emissive devices? *Org. Electron.* **2015**, *21*, 27–39. [[CrossRef](#)]
23. Ravaro, L.P.; Zanon, K.P.S.; de Camargo, A.S.S. Luminescent Copper(I) complexes as promising materials for the next generation of energy-saving OLED devices. *Energy Rep.* **2020**, *6*, 37–45. [[CrossRef](#)]
24. Housecroft, C.E.; Constable, E.C. TADF: Enabling luminescent copper(I) coordination compounds for light-emitting electrochemical cells. *J. Mater. Chem. C* **2022**, *10*, 4456–4482. [[CrossRef](#)] [[PubMed](#)]
25. Cariati, E.; Lucenti, E.; Botta, C.; Giovanella, U.; Marinotto, D.; Righetto, S. Cu(I) hybrid inorganic–organic materials with intriguing stimuli responsive and optoelectronic properties. *Coord. Chem. Rev.* **2016**, *306*, 566–614. [[CrossRef](#)]
26. Kiracki, K.; Fejfarová, K.; Martinčík, J.; Nikl, M.; Lang, K. Tetranuclear Copper(I) Iodide Complexes: A New Class of X-ray Phosphors. *Inorg. Chem.* **2017**, *56*, 4609–4614. [[CrossRef](#)]
27. Conesa-Egea, J.; Zamora, F.; Amo-Ochoa, P. Perspectives of the smart Cu-Iodine coordination polymers: A portage to the world of new nanomaterials and composites. *Coord. Chem. Rev.* **2019**, *381*, 65–78. [[CrossRef](#)]
28. Evariste, S.; Khalil, A.M.; Kerneis, S.; Xu, C.; Calvez, G.; Costuas, K.; Lescop, C. Luminescent vapochromic single crystal to single crystal transition in one-dimensional coordination polymer featuring the first Cu(I) dimer bridged by an aqua ligand. *Inorg. Chem. Front.* **2020**, *7*, 3402–3411. [[CrossRef](#)]
29. Paderina, A.V.; Koshevoy, I.O.; Grachova, E.V. Keep it tight: A crucial role of bridging phosphine ligands in the design and optical properties of multinuclear coinage metal complexes. *Dalton Trans.* **2021**, *50*, 6003–6033. [[CrossRef](#)]
30. Conaghan, P.J.; Matthews, C.S.B.; Chotard, F.; Jones, S.T.E.; Greenham, N.C.; Bochmann, M.; Credgington, D.; Romanov, A.S. Highly efficient blue organic light-emitting diodes based on carbene-metal-amides. *Nat. Commun.* **2020**, *11*, 1758. [[CrossRef](#)]
31. Kobayashi, A.; Ehara, T.; Yoshida, M.; Kato, M. Quantitative Thermal Synthesis of Cu(I) Coordination Polymers That Exhibit Thermally Activated Delayed Fluorescence. *Inorg. Chem.* **2020**, *59*, 9511–9520. [[CrossRef](#)]
32. Kirst, C.; Tietze, J.; Mayer, P.; Böttcher, H.-C.; Karaghiosoff, K. Coinage Metal Complexes of Bis(quinoline-2-ylmethyl)phenylphosphine—Simple Reactions Can Lead to Unprecedented Results. *ChemistryOpen* **2022**, *11*, e202100224. [[CrossRef](#)] [[PubMed](#)]
33. Kirst, C.; Zoller, F.; Bräuniger, T.; Mayer, P.; Fattakhova-Rohlfing, D.; Karaghiosoff, K. Investigation of Structural Changes of Cu(I) and Ag(I) Complexes Utilizing a Flexible, Yet Sterically Demanding Multidentate Phosphine Oxide Ligand. *Inorg. Chem.* **2021**, *60*, 2437–2445. [[CrossRef](#)] [[PubMed](#)]

34. Khalil, A.M.; Xu, C.; Delmas, V.; Calvez, G.; Costuas, K.; Haouas, M.; Lescop, C. Coordination-driven supramolecular syntheses of new homo- and hetero-polymetallic Cu(I) assemblies: Solid-state and solution characterization. *Inorg. Chem. Front.* **2021**, *8*, 4887–4895. [[CrossRef](#)]
35. Galimova, M.F.; Zueva, E.M.; Dobrynin, A.B.; Samigullina, A.I.; Musin, R.R.; Musina, E.I.; Karasik, A.A. Cu₄I₄-cubane clusters based on 10-(aryl)phenoxarsines and their luminescence. *Dalton Trans.* **2020**, *49*, 482–491. [[CrossRef](#)] [[PubMed](#)]
36. Galimova, M.F.; Zueva, E.M.; Dobrynin, A.B.; Kolesnikov, I.E.; Musin, R.R.; Musina, E.I.; Karasik, A.A. Luminescent Cu₄I₄-cubane clusters based on *N*-methyl-5,10-dihydrophenarsazines. *Dalton Trans.* **2021**, *50*, 13421–13429. [[CrossRef](#)]
37. Kobayashi, R.; Kihara, H.; Kusakawa, T.; Imoto, H.; Naka, K. Dinuclear Rhombic Copper(I) Iodide Complexes with Rigid Bidentate Arsenic Ligands. *Chem. Lett.* **2021**, *50*, 382–385. [[CrossRef](#)]
38. Artem'ev, A.V.; Demyanov, Y.V.; Rakhmanova, M.I.; Bagryanskaya, I.Y. Pyridylarsine-based Cu(I) complexes showing TADF mixed with fast phosphorescence: A speeding-up emission rate using arsine ligands. *Dalton Trans.* **2022**, *51*, 1048–1055. [[CrossRef](#)]
39. Montalti, M.; Credi, A.; Prodi, L.; Gandolfi, M.T. *Handbook of Photochemistry*, 3rd ed.; CRC Press: Boca Raton, FL, USA, 2006; p. 633.
40. Wallesch, M.; Volz, D.; Zink, D.M.; Schepers, U.; Nieger, M.; Baumann, T.; Bräse, S. Bright Coppertunities: Multinuclear Cu^I Complexes with N–P Ligands and Their Applications. *Chem. Eur. J.* **2014**, *20*, 6578–6590. [[CrossRef](#)]
41. Zink, D.M.; Bächle, M.; Baumann, T.; Nieger, M.; Kühn, M.; Wang, C.; Klopper, W.; Monkowius, U.; Hofbeck, T.; Yersin, H.; et al. Synthesis, Structure, and Characterization of Dinuclear Copper(I) Halide Complexes with P[∞]N Ligands Featuring Exciting Photoluminescence Properties. *Inorg. Chem.* **2013**, *52*, 2292–2305. [[CrossRef](#)]
42. Cheng, G.; Zhou, D.; Monkowius, U.; Yersin, H. Fabrication of a Solution-Processed White Light Emitting Diode Containing a Single Dimeric Copper(I) Emitter Featuring Combined TADF and Phosphorescence. *Micromachines* **2021**, *12*, 1500. [[CrossRef](#)] [[PubMed](#)]
43. Hofbeck, T.; Niehaus, T.A.; Fleck, M.; Monkowius, U.; Yersin, H. P[∞]N Bridged Cu(I) Dimers Featuring Both TADF and Phosphorescence. From Overview towards Detailed Case Study of the Excited Singlet and Triplet States. *Molecules* **2021**, *26*, 3415. [[CrossRef](#)] [[PubMed](#)]
44. Hofbeck, T.; Monkowius, U.; Yersin, H. Highly Efficient Luminescence of Cu(I) Compounds: Thermally Activated Delayed Fluorescence Combined with Short-Lived Phosphorescence. *J. Am. Chem. Soc.* **2015**, *137*, 399–404. [[CrossRef](#)]
45. Kobayashi, R.; Fujii, T.; Imoto, H.; Naka, K. Dinuclear Gold(I) Chloride Complexes with Diarsine Ligands. *Eur. J. Inorg. Chem.* **2021**, 217–222. [[CrossRef](#)]
46. Plajer, A.J.; Crusius, D.; Jethwa, R.B.; García-Romero, Á.; Bond, A.D.; García-Rodríguez, R.; Wright, D.S. Coordination chemistry of the bench-stable tris-2-pyridyl pnictogen ligands [E(6-Me-2-py)₃] (E = As, As=O, Sb). *Dalton Trans.* **2021**, *50*, 2393–2402. [[CrossRef](#)] [[PubMed](#)]
47. Gneuß, T.; Leitl, M.J.; Finger, L.H.; Yersin, H.; Sundermeyer, J. A new class of deep-blue emitting Cu(I) compounds—effects of counter ions on the emission behavior. *Dalton Trans.* **2015**, *44*, 20045–20055. [[CrossRef](#)]
48. Baranov, A.; Berezin, A.S.; Samsonenko, D.G.; Mazur, A.; Tolstoy, P.; Plyusnin, V.F.; Kolesnikov, I.E.; Artem'ev, A. New Cu(I) halide complexes showing TADF combined with room temperature phosphorescence: The balance tuned by halogens. *Dalton Trans.* **2020**, *49*, 3155–3163. [[CrossRef](#)]
49. Yang, L.; Powell, D.R.; Houser, R.P. Structural variation in copper(I) complexes with pyridylmethylamide ligands: Structural analysis with a new four-coordinate geometry index, τ_4 . *Dalton Trans.* **2007**, 955–964. [[CrossRef](#)]
50. Gneuß, T.; Leitl, M.J.; Finger, L.H.; Rau, N.; Yersin, H.; Sundermeyer, J. A new class of luminescent Cu(I) complexes with tripodal ligands—TADF emitters for the yellow to red color range. *Dalton Trans.* **2015**, *44*, 8506–8520. [[CrossRef](#)]
51. Bondi, A. van der Waals Volumes and Radii. *J. Phys. Chem.* **1964**, *68*, 441–451. [[CrossRef](#)]
52. Artem'ev, A.V.; Bagryanskaya, I.Y.; Doronina, E.P.; Tolstoy, P.M.; Gushchin, A.L.; Rakhmanova, M.I.; Ivanov, A.Y.; Suturina, A.O. A new family of clusters containing a silver-centered tetracapped [Ag@Ag₄(μ₃-P)₄] tetrahedron, inscribed within a N₁₂ icosahedron. *Dalton Trans.* **2017**, *46*, 12425–12429. [[CrossRef](#)] [[PubMed](#)]
53. Kolari, K.; Sahamies, J.; Kalenius, E.; Novikov, A.S.; Kukushkin, V.Y.; Haukka, M. Metallophilic interactions in polymeric group 11 thiols. *Solid State Sci.* **2016**, *60*, 92–98. [[CrossRef](#)]
54. Andrusenko, E.V.; Kabin, E.V.; Novikov, A.S.; Bokach, N.A.; Starova, G.L.; Kukushkin, V.Y. Metal-mediated Generation of Triazapentadienate-terminated Di- and Trinuclear μ₂-Pyrazolate Ni^{II} Species and Control of their Nuclearity. *New J. Chem.* **2017**, *41*, 316–325. [[CrossRef](#)]
55. Bikbaeva, Z.M.; Novikov, A.S.; Suslonov, V.V.; Bokach, N.A.; Kukushkin, V.Y. Metal-mediated reactions between dialkylcyanamides and acetamidoxime generate unusual (nitrosoguanidinate)nickel(II) complexes. *Dalton Trans.* **2017**, *46*, 10090–10101. [[CrossRef](#)]
56. Novikov, A.S. Strong metallophilic interactions in nickel coordination compounds. *Inorg. Chim. Acta* **2018**, *483*, 21–25. [[CrossRef](#)]
57. Shmelev, N.Y.; Okubazghi, T.H.; Abramov, P.A.; Komarov, V.Y.; Rakhmanova, M.I.; Novikov, A.S.; Gushchin, A.L. Intramolecular aurophilic interactions in dinuclear gold(I) complexes with twisted bridging 2,2'-bipyridine ligands. *Dalton Trans.* **2021**, *50*, 12448–12456. [[CrossRef](#)]
58. Grudova, M.V.; Novikov, A.S.; Kubasov, A.S.; Khrustalev, V.N.; Kirichuk, A.A.; Nenajdenko, V.G.; Tskhovrebov, A.G. Aurophilic Interactions in Cationic Three-Coordinate Gold(I) Bipyridyl/Isocyanide Complex. *Crystals* **2022**, *12*, 613. [[CrossRef](#)]

59. Shmelev, N.Y.; Okubazghi, T.H.; Abramov, P.A.; Rakhmanova, M.I.; Novikov, A.S.; Sokolov, M.N.; Gushchin, A.L. Asymmetric Coordination Mode of Phenanthroline-like Ligands in Gold(I) Complexes: A Case of the Antichelate Effect. *Cryst. Growth Des.* **2022**, *22*, 3882–3895. [[CrossRef](#)]
60. Espinosa, E.; Alkorta, I.; Elguero, J.; Molins, E. From weak to strong interactions: A comprehensive analysis of the topological and energetic properties of the electron density distribution involving X–HF–Y systems. *J. Chem. Phys.* **2002**, *117*, 5529–5542. [[CrossRef](#)]
61. Johnson, E.R.; Keinan, S.; Mori-Sánchez, P.; Contreras-García, J.; Cohen, A.J.; Yang, W. Revealing Noncovalent Interactions. *J. Am. Chem. Soc.* **2010**, *132*, 6498–6506. [[CrossRef](#)]
62. Contreras-García, J.; Johnson, E.R.; Keinan, S.; Chaudret, R.; Piquemal, J.-P.; Beratan, D.N.; Yang, W. NCIPLOT: A Program for Plotting Noncovalent Interaction Regions. *J. Chem. Theory Comput.* **2011**, *7*, 625–632. [[CrossRef](#)] [[PubMed](#)]
63. Kobayashi, A.; Hasegawa, T.; Yoshida, M.; Kato, M. Environmentally Friendly Mechanochemical Syntheses and Conversions of Highly Luminescent Cu(I) Dinuclear Complexes. *Inorg. Chem.* **2016**, *55*, 1978–1985. [[CrossRef](#)] [[PubMed](#)]
64. Sheldrick, G.M. Crystal structure refinement with SHELXL. *Acta Cryst. A* **2015**, *71*, 3–8. [[CrossRef](#)] [[PubMed](#)]
65. *Bruker Apex3 Software Suite: Apex3, SADABS-2016/2 and SAINT*, version 2018.7-2; Bruker AXS Inc.: Madison, WI, USA, 2017.
66. Frisch, M.; Trucks, G.W.; Schlegel, H.B.; Scuseria, G.E.; Robb, M.A.; Cheeseman, J.R.; Scalmani, G.; Barone, V.; Mennucci, B.; Petersson, G.A.; et al. *Gaussian 09, Revision C.01*; Gaussian, Inc.: Wallingford, CT, USA, 2010.
67. Adamo, C.; Barone, V. Toward reliable density functional methods without adjustable parameters: The PBE0 model. *J. Chem. Phys.* **1999**, *110*, 6158–6170. [[CrossRef](#)]
68. Perdew, J.P.; Burke, K.; Ernzerhof, M. Generalized gradient approximation made simple. *Phys. Rev. Lett.* **1996**, *77*, 3865–3868. [[CrossRef](#)]
69. Pritchard, B.P.; Altarawy, D.; Didier, B.; Gibson, T.D.; Windus, T.L. New basis set exchange: An open, up-to-date resource for the molecular sciences community. *J. Chem. Inf. Model* **2019**, *59*, 4814–4820. [[CrossRef](#)]
70. Bauernschmitt, R.; Ahlrichs, R. Treatment of electronic excitations within the adiabatic approximation of time dependent density functional theory. *Chem. Phys. Lett.* **1996**, *256*, 454–464. [[CrossRef](#)]
71. Van Caillie, C.; Amos, R.D. Geometric derivatives of excitation energies using SCF and DFT. *Chem. Phys. Lett.* **1999**, *308*, 249–255. [[CrossRef](#)]
72. Scalmani, G.; Frisch, M.J.; Mennucci, B.; Tomasi, J.; Cammi, R.; Barone, V. Geometries and properties of excited states in the gas phase and in solution: Theory and application of a time-dependent density functional theory polarizable continuum model. *J. Chem. Phys.* **2006**, *124*, 094107. [[CrossRef](#)]
73. Chai, J.D.; Head-Gordon, M. Long-range corrected hybrid density functionals with damped atom–atom dispersion corrections. *Phys. Chem. Chem. Phys.* **2008**, *10*, 6615–6620. [[CrossRef](#)]
74. Barros, C.L.; De Oliveira, P.J.P.; Jorge, F.E.; Canal Neto, A.; Campos, M. Gaussian basis set of double zeta quality for atoms Rb through Xe: Application in non-relativistic and relativistic calculations of atomic and molecular properties. *Mol. Phys.* **2010**, *108*, 1965–1972. [[CrossRef](#)]
75. Jorge, F.E.; Canal Neto, A.; Camiletti, G.G.; Machado, S.F. Contracted Gaussian basis sets for Douglas–Kroll–Hess calculations: Estimating scalar relativistic effects of some atomic and molecular properties. *J. Chem. Phys.* **2009**, *130*, 064108. [[CrossRef](#)] [[PubMed](#)]
76. Neto, A.C.; Jorge, F.E. All-electron double zeta basis sets for the most fifth-row atoms: Application in DFT spectroscopic constant calculations. *Chem. Phys. Lett.* **2013**, *582*, 158–162. [[CrossRef](#)]
77. De Berrêdo, R.C.; Jorge, F.E. All-electron double zeta basis sets for platinum: Estimating scalar relativistic effects on platinum (II) anticancer drugs. *J. Mol. Struct. Theochem.* **2010**, *961*, 107–112. [[CrossRef](#)]
78. Lu, T.; Chen, F. Multiwfn: A multifunctional wavefunction analyzer. *J. Comput. Chem.* **2012**, *33*, 580–592. [[CrossRef](#)] [[PubMed](#)]